

Dark Matter Search Results from 4.2 Tonne-Years of Exposure of the LUX-ZEPLIN (LZ) Experiment

J. Aalbers,^{1,2} D.S. Akerib,^{1,2} A.K. Al Musalhi,³ F. Alder,³ C.S. Amarasinghe,⁴ A. Ames,^{1,2} T.J. Anderson,^{1,2}
 N. Angelides,⁵ H.M. Araújo,⁵ J.E. Armstrong,⁶ M. Arthurs,^{1,2} A. Baker,⁷ S. Balashov,⁸ J. Bang,⁹
 J.W. Bargemann,⁴ E.E. Barillier,^{10,11} D. Bauer,⁵ K. Beattie,¹² T. Benson,¹³ A. Bhatti,⁶ A. Biekert,^{12,14}
 T.P. Biesiadzinski,^{1,2} H.J. Birch,^{10,11} E. Bishop,¹⁵ G.M. Blockinger,¹⁶ B. Boxer,¹⁷ C.A.J. Brew,⁸ P. Brás,¹⁸
 S. Burdin,¹⁹ M. Buuck,^{1,2} M.C. Carmona-Benitez,²⁰ M. Carter,¹⁹ A. Chawla,²¹ H. Chen,¹² J.J. Cherwinka,¹³
 Y.T. Chin,²⁰ N.I. Chott,²² M.V. Converse,²³ R. Coronel,^{1,2} A. Cottle,^{3,*} G. Cox,²⁴ D. Curran,²⁴ C.E. Dahl,^{25,26}
 I. Darlington,³ S. Dave,³ A. David,³ J. Delgado,²⁴ S. Dey,²⁷ L. de Viveiros,²⁰ L. Di Felice,⁵ C. Ding,⁹
 J.E.Y. Dobson,⁷ E. Druskiewicz,²³ S. Dubey,⁹ S.R. Eriksen,²⁸ A. Fan,^{1,2} S. Fayer,⁵ N.M. Fearon,²⁷
 N. Fieldhouse,²⁷ S. Fiorucci,¹² H. Flaecher,²⁸ E.D. Fraser,¹⁹ T.M.A. Fruth,²⁹ R.J. Gaitskill,⁹ A. Geffre,²⁴
 J. Genovesi,²² C. Ghag,³ A. Ghosh,¹⁶ R. Gibbons,^{12,14} S. Gokhale,³⁰ J. Green,²⁷ M.G.D. van der Grinten,⁸
 J.J. Haiston,²² C.R. Hall,⁶ T.J. Hall,¹⁹ S. Han,^{1,2} E. Hartigan-O'Connor,⁹ S.J. Haselschwardt,^{10,12,†}
 M.A. Hernandez,^{10,11} S.A. Hertel,³¹ G. Heuermann,¹⁰ G.J. Homenides,³² M. Horn,²⁴ D.Q. Huang,³³ D. Hunt,²⁷
 E. Jacquet,⁵ R.S. James,^{3,‡} J. Johnson,¹⁷ A.C. Kaboth,²¹ A.C. Kamaha,³³ Meghna K.K.,¹⁶ D. Khaitan,²³
 A. Khazov,⁸ I. Khurana,³ J. Kim,⁴ Y.D. Kim,³⁴ J. Kingston,¹⁷ R. Kirk,⁹ D. Kodroff,¹² L. Korley,¹⁰
 E.V. Korolkova,³⁵ H. Kraus,²⁷ S. Kravitz,³⁶ L. Kreczko,²⁸ V.A. Kudryavtsev,³⁵ C. Lawes,⁷ D.S. Leonard,³⁴
 K.T. Lesko,¹² C. Levy,¹⁶ J. Lin,^{12,14} A. Lindote,¹⁸ W.H. Lippincott,⁴ M.I. Lopes,¹⁸ W. Lorenzon,¹⁰ C. Lu,⁹
 S. Luitz,^{1,37} P.A. Majewski,⁸ A. Manalaysay,¹² R.L. Mannino,³⁸ C. Maupin,²⁴ M.E. McCarthy,²³ G. McDowell,¹⁰
 D.N. McKinsey,^{12,14} J. McLaughlin,²⁵ J.B. McLaughlin,³ R. McMonigle,¹⁶ E. Mizrahi,^{6,38} A. Monte,⁴
 M.E. Monzani,^{1,2,39} J.D. Morales Mendoza,^{1,2} E. Morrison,²² B.J. Mount,⁴⁰ M. Murdy,³¹ A.St.J. Murphy,¹⁵
 A. Naylor,³⁵ H.N. Nelson,⁴ F. Neves,¹⁸ A. Nguyen,¹⁵ C.L. O'Brien,³⁶ I. Olcina,^{12,14} K.C. Oliver-Mallory,⁵
 J. Orpwood,³⁵ K.Y. Oyulmaz,¹⁵ K.J. Palladino,²⁷ J. Palmer,²¹ N.J. Pannifer,²⁸ N. Parveen,¹⁶ S.J. Patton,¹²
 B. Penning,^{10,11} G. Pereira,¹⁸ E. Perry,³ T. Pershing,³⁸ A. Piepke,³² Y. Qie,²³ J. Reichenbacher,²² C.A. Rhyne,⁹
 A. Richards,⁵ Q. Riffard,¹² G.R.C. Rischbieter,^{10,11} E. Ritchey,⁶ H.S. Riyat,¹⁵ R. Rosero,³⁰ T. Rushton,³⁵
 D. Rynders,²⁴ D. Santone,²¹ A.B.M.R. Sazzad,³² R.W. Schnee,²² G. Sehr,³⁶ B. Shafer,⁶ S. Shaw,¹⁵ T. Shutt,^{1,2}
 J.J. Silk,⁶ C. Silva,¹⁸ G. Sinev,²² J. Siniscalco,³ R. Smith,^{12,14} V.N. Solovov,¹⁸ P. Sorensen,¹² J. Soria,^{12,14}
 I. Stancu,³² A. Stevens,^{3,5} K. Stifter,²⁶ B. Suerfu,^{12,14} T.J. Sumner,⁵ M. Szydagis,¹⁶ D.R. Tiedt,²⁴ M. Timalaina,¹²
 Z. Tong,⁵ D.R. Tovey,³⁵ J. Tranter,³⁵ M. Trask,⁴ M. Tripathi,¹⁷ A. Usón,¹⁵ A. Vacheret,⁵ A.C. Vaitkus,⁹
 O. Valentino,⁵ V. Velan,¹² A. Wang,^{1,2} J.J. Wang,³² Y. Wang,^{12,14} J.R. Watson,^{12,14} L. Weeldreyer,³²
 T.J. Whitis,⁴ K. Wild,²⁰ M. Williams,¹⁰ W.J. Wisniewski,¹ L. Wolf,²¹ F.L.H. Wolfs,²³ S. Woodford,¹⁹
 D. Woodward,^{12,20} C.J. Wright,²⁸ Q. Xia,¹² J. Xu,³⁸ Y. Xu,³³ M. Yeh,³⁰ D. Yeum,⁶ W. Zha,²⁰ and E.A. Zweig³³

(The LZ Collaboration)

¹SLAC National Accelerator Laboratory, Menlo Park, CA 94025-7015, USA

²Kavli Institute for Particle Astrophysics and Cosmology,
Stanford University, Stanford, CA 94305-4085, USA

³University College London (UCL), Department of Physics and Astronomy, London WC1E 6BT, UK

⁴University of California, Santa Barbara, Department of Physics, Santa Barbara, CA 93106-9530, USA

⁵Imperial College London, Physics Department, Blackett Laboratory, London SW7 2AZ, UK

⁶University of Maryland, Department of Physics, College Park, MD 20742-4111, USA

⁷King's College London, Department of Physics, London WC2R 2LS, UK

⁸STFC Rutherford Appleton Laboratory (RAL), Didcot, OX11 0QX, UK

⁹Brown University, Department of Physics, Providence, RI 02912-9037, USA

¹⁰University of Michigan, Randall Laboratory of Physics, Ann Arbor, MI 48109-1040, USA

¹¹University of Zürich, Department of Physics, 8057 Zürich, Switzerland

¹²Lawrence Berkeley National Laboratory (LBNL), Berkeley, CA 94720-8099, USA

¹³University of Wisconsin-Madison, Department of Physics, Madison, WI 53706-1390, USA

¹⁴University of California, Berkeley, Department of Physics, Berkeley, CA 94720-7300, USA

¹⁵University of Edinburgh, SUPA, School of Physics and Astronomy, Edinburgh EH9 3FD, UK

¹⁶University at Albany (SUNY), Department of Physics, Albany, NY 12222-0100, USA

¹⁷University of California, Davis, Department of Physics, Davis, CA 95616-5270, USA

¹⁸Laboratório de Instrumentação e Física Experimental de Partículas (LIP),
University of Coimbra, P-3004 516 Coimbra, Portugal

¹⁹University of Liverpool, Department of Physics, Liverpool L69 7ZE, UK

- ²⁰*Pennsylvania State University, Department of Physics, University Park, PA 16802-6300, USA*
²¹*Royal Holloway, University of London, Department of Physics, Egham, TW20 0EX, UK*
²²*South Dakota School of Mines and Technology, Rapid City, SD 57701-3901, USA*
²³*University of Rochester, Department of Physics and Astronomy, Rochester, NY 14627-0171, USA*
²⁴*South Dakota Science and Technology Authority (SDSTA),
Sanford Underground Research Facility, Lead, SD 57754-1700, USA*
²⁵*Northwestern University, Department of Physics & Astronomy, Evanston, IL 60208-3112, USA*
²⁶*Fermi National Accelerator Laboratory (FNAL), Batavia, IL 60510-5011, USA*
²⁷*University of Oxford, Department of Physics, Oxford OX1 3RH, UK*
²⁸*University of Bristol, H.H. Wills Physics Laboratory, Bristol, BS8 1TL, UK*
²⁹*The University of Sydney, School of Physics, Physics Road, Camperdown, Sydney, NSW 2006, Australia*
³⁰*Brookhaven National Laboratory (BNL), Upton, NY 11973-5000, USA*
³¹*University of Massachusetts, Department of Physics, Amherst, MA 01003-9337, USA*
³²*University of Alabama, Department of Physics & Astronomy, Tuscaloosa, AL 3587-0324, USA*
³³*University of California, Los Angeles, Department of Physics & Astronomy, Los Angeles, CA 90095-1547, USA*
³⁴*IBS Center for Underground Physics (CUP), Yuseong-gu, Daejeon, Korea*
³⁵*University of Sheffield, Department of Physics and Astronomy, Sheffield S3 7RH, UK*
³⁶*University of Texas at Austin, Department of Physics, Austin, TX 78712-1192, USA*
³⁷*Kavli Institute for Particle Astrophysics and Cosmology,
Stanford University, Stanford, CA 94305-4085 USA*
³⁸*Lawrence Livermore National Laboratory (LLNL), Livermore, CA 94550-9698, USA*
³⁹*Vatican Observatory, Castel Gandolfo, V-00120, Vatican City State*
⁴⁰*Black Hills State University, School of Natural Sciences, Spearfish, SD 57799-0002, USA*

We report results of a search for nuclear recoils induced by weakly interacting massive particle (WIMP) dark matter using the LUX-ZEPLIN (LZ) two-phase xenon time projection chamber. This analysis uses a total exposure of 4.2 ± 0.1 tonne-years from 280 live days of LZ operation, of which 3.3 ± 0.1 tonne-years and 220 live days are new. A technique to actively tag background electronic recoils from ^{214}Pb β decays is featured for the first time. Enhanced electron-ion recombination is observed in two-neutrino double electron capture decays of ^{124}Xe , representing a noteworthy new background. After removal of artificial signal-like events injected into the data set to mitigate analyzer bias, we find no evidence for an excess over expected backgrounds. World-leading constraints are placed on spin-independent (SI) and spin-dependent WIMP-nucleon cross sections for masses ≥ 9 GeV/c^2 . The strongest SI exclusion set is 2.1×10^{-48} cm^2 at the 90% confidence level at a mass of 36 GeV/c^2 , and the best SI median sensitivity achieved is 5.0×10^{-48} cm^2 for a mass of 40 GeV/c^2 .

Astrophysical observations provide strong evidence for the existence of dark matter and its dominance of the matter density of the Universe [1–4]. Well-motivated as a thermal relic, the weakly interacting massive particle (WIMP) is a leading hypothesis for dark matter, arising in a number of beyond-the-standard-model theories [5–7]. The LUX-ZEPLIN (LZ) collaboration operates the world’s largest two-phase xenon time projection chamber (TPC), with the primary aim of directly detecting WIMPs through their interactions with xenon nuclei. This technology has produced the most stringent constraints on spin-independent (SI) WIMP-nucleon interactions for $\gtrsim 5$ GeV/c^2 masses, with all three current-generation experiments having reported first results [8–10]. In this Letter we present the latest WIMP analysis from LZ, combining a new 220 live-day exposure (WS2024) with the 60 live-day exposure from the first result (WS2022) [8] to perform the most sensitive direct search for WIMPs to date.

The LZ experiment [11] is located 4850 ft underground, shielded by a 4300 meter water equivalent rock overburden in the Davis Cavern at the Sanford Underground Research Facility (SURF) in Lead, South Dakota, USA.

Its TPC, containing seven tonnes of active liquid xenon (LXe), is surrounded by a dual-detector veto system comprising a two-tonne LXe “Skin,” designed to tag γ rays, and an outer detector (OD) containing 17 tonnes of gadolinium-loaded liquid scintillator (GdLS), optimized for the detection of neutrons.

Interactions in the LXe target that fills the TPC create light in the form of prompt vacuum ultraviolet (VUV) scintillation (S1) and delayed electroluminescence (S2), both observed by the top and bottom photomultiplier tube (PMT) arrays. The S2 signal is generated by ionization electrons as they traverse a thin layer of gaseous xenon above the liquid, having been drifted upwards from the interaction site under an applied electric field and extracted from the liquid phase. The measured time interval between the S1 and the S2 pulses, referred to as the “drift time”, corresponds to the depth, z , of the interaction, while the hit pattern of S2 light in the top PMT array allows for position reconstruction in the transverse (x, y) plane. The ratio of S2 to S1 signal sizes is used to discriminate between background electronic recoils (ERs) and nuclear recoils (NRs), the latter of which is expected for WIMP-nucleus scatters. Background events are fur-

ther rejected if they exhibit multiple scatters (MS) rather than a single scatter (SS) in the TPC, or through the presence of coincident signals in the Skin and/or OD.

The LXe target is contained in a vacuum-insulated cryostat, and is continuously circulated for gas-phase purification to remove electronegative impurities, and to regulate the liquid level. The cooling and circulation systems allow for control of the LXe flow pattern inside the cryostat, which influences the spatial distribution and movement of radioisotopes in the TPC volume. Two distinct flow configurations can be attained, referred to as the “high-mixing” and “low-mixing” states. In the high-mixing state, the liquid flow results in spatially homogeneous distributions of injected calibration sources. In the low-mixing state, there exist distinct regions of laminar flow throughout the detector, and coincident ^{222}Rn – ^{218}Po α decays can be reliably used to map the LXe velocity field. The ability to model the flow in this state is exploited in the development of a “radon tag” to target the prominent ^{214}Pb ER background (similar to that in Ref. [12]), discussed later.

Cathode, gate, and anode electrodes establish the TPC drift field at 97 V/cm and the liquid-gas extraction field at 3.4 kV/cm (at the radial center, below the liquid surface) for the WS2024 data-taking campaign. With respect to WS2022, the extraction field was decreased to reduce the dead time incurred from spurious electron and photon emission, and the cathode voltage was lowered in response to the onset of persistent light emission localized to the Skin region below the cathode.

This analysis incorporates 220.0 live days collected in the new electrode bias configuration between March 27, 2023 and April 1, 2024. Of this WS2024 live time, 40.9 live days are included from when the detector is in the high-mixing state, due to proximity to injected calibrations, with the remaining 179.1 live days taken in the low-mixing state. The xenon gas pressure throughout the run is 1.860 bar(a) with variation at the level of 0.03%. The level of convective mixing is controlled by adjusting the temperature of the liquid returning to the bottom of the TPC from 177.9 K (high-mixing state) to 174.2 K (low-mixing state), with variations at the level of 0.02% for each. Changing from high-mixing to low-mixing state increases the maximum drift time from 1045 μs to 1050 μs and reduces the overall liquid height by about 0.2 mm. The consequent 1% increase in S2 signal size is corrected for in analysis.

Data acquisition uses a trigger with a digital filter designed primarily to capture S2 pulses. The trigger was optimized for WS2024 to increase the sensitivity to low-energy events of interest to the WIMP analysis, achieving an efficiency of 95% for S2 pulses corresponding to 3.5 extracted electrons. Waveforms from the TPC, Skin, and OD PMTs are recorded with a window extending from 2.2 ms before the trigger time to 2.5 ms after it, sampled at 100 MHz. Further details of the data acquisition and

signal chain are described in Ref. [13].

Event waveforms are processed to find and categorize pulses and interactions. Pulse sizes are normalized by the time-dependent size of single VUV photon pulses measured in each channel, and are reported as the number of photons detected (phd) [14, 15]. Events are categorized as SS if they have a single S1 preceding a single S2. The SS identification efficiency is dependent on the S1 and S2 pulse classification efficiencies. Ionization electrons diffuse as they drift, which can lead to fragmentation of the S2 signal into multiple pulses. The splitting probability is <1% on average across the TPC for S2 pulses relevant to this analysis, as estimated with waveform simulations [16]. For a pulse to be classified as S1, coincident photons must be recorded in at least three PMTs; however, undersized PMT responses and differences in photon transit times can lead to missed S1 pulses. The SS S1 identification efficiency is found to be >90% for all S1 pulse sizes in this analysis, rising to 100% for S1s >35 phd (8 keV). This efficiency is assessed by comparing the event classification of a sample of tritium and deuterium-deuterium (DD) neutron calibration events determined by the event reconstruction algorithms to the corresponding classification obtained from a manual, visual categorization campaign.

Tritium and DD neutrons are among several sources used to calibrate the TPC [17]. Tritium is delivered through radiolabeled methane along with ^{14}C , in an activity ratio of approximately 8:1. The tritiated methane, primarily used to calibrate the ER response, was injected into the TPC while in the high-mixing state to ensure its efficient dispersal and complete removal. Mono-energetic 2.45 MeV neutrons from a collimated DD generator, directed roughly 10 cm below the LXe surface, supply the counterpart for calibrating the NR response. AmLi neutron sources, deployed in source tubes at three different azimuthal positions and three different heights around the TPC, provide additional NR calibration events. Injections of $^{131\text{m}}\text{Xe}$ and $^{83\text{m}}\text{Kr}$ at roughly monthly and trimonthly cadences, respectively, in addition to background radon progeny, provide mono-energetic peaks throughout WS2024, used to monitor the stability of the detector response and develop corrections for the normalization of S1 and S2 signals.

S1 and S2 signals exhibit spatial and temporal variations due to factors such as changing detector conditions or non-uniform light collection and electron extraction efficiencies. Corrections are applied to produce standardized values, S1c and S2c. An (x, y, z) map normalizes the S1 signals to the center of the TPC volume, with correction factors averaging 8% in absolute value. S2 signals are normalized to the radial center of the liquid surface in the (x, y) plane, in addition to being corrected for the depth-dependent probability of electron attachment to electronegative impurities in the LXe; the average values of these corrections are approximately 13% and 7%,

respectively. The responses are also normalized in time, using the tritium calibration period as the reference.

Calibrations also inform the tuning of the NEST 2.4.0 [18] model for detector response, in which the scintillation photon and ionization electron gains, g_1 and g_2 , are key parameters. A scan over viable values for g_1 and g_2 , performed using tritium data in $\{S1c, \log_{10}(S2c)\}$ space and constrained by the energy reconstruction of ^{131m}Xe and ^{83m}Kr peaks, yields $g_1 = 0.112 \pm 0.002$ phd/photon and $g_2 = 34.0 \pm 0.9$ phd/electron. A further tuning to more accurately capture the “ER band,” i.e. the shape of the observed distribution of tritium data, enables NEST to reproduce the band median and width to better than 0.2% and 5% in $\log_{10}(S2c)$, respectively. The DD data define an analogous “NR band,” for which NEST is separately tuned to a similar level of precision via small adjustments in the NR yield parameters. The DD neutron interactions are confined to the top of the detector, where the average electric field is 7% higher than the center. Because the charge yield of ^{222}Rn α decays used for spatial corrections is more field-sensitive than NRs, corrections in the DD neutron region overestimate field effects on recombination, leading to a systematic shift in the NR band position as assumed for the full TPC. An upwards shift of 2.4% in $S2c$ is applied to the NR model to compensate for this effect, calculated from electrostatic simulations and NEST-based models.

Candidate events for the WIMP analysis are selected if they are classified as SS; they are located within the fiducial volume (FV); they pass veto coincidence, S1 and S2-based, and live-time exclusion cuts, all of which are described below; and they lie within the WIMP region of interest (ROI). The ROI is defined such that the corrected S1 and S2 pulse sizes are in the range of $3 < S1c < 80$ phd and $\log_{10}(S2c) < 4.5$. A lower bound on uncorrected S2 pulse size of 645 phd, equivalent to 14.5 extracted electrons, is also applied. This S2 threshold renders the analysis largely insensitive to ^8B coherent elastic neutrino-nucleus scattering (CE ν NS), a search for which will be reported in a future publication.

A FV, illustrated in Fig. 1, is defined to suppress external backgrounds. Drift time limits are placed at 71 μs and 1034 (1030) μs in the low(high)-mixing state, corresponding to distances of 9.9 cm below the gate and 2.2 cm above the cathode, respectively. Events within 6.0 cm of the TPC field cage resistors [11] in (x, y) are also excluded, as these resistors have elevated radioactivity. The radial fiducial boundary is defined such that backgrounds originating from the TPC wall, which can be misreconstructed radially inwards due to finite position resolution, have a negligible expectation of < 0.01 events for WS2024. This radial boundary follows a contour of measured wall background event rate, and is a function of both depth and azimuthal angle. The fiducial mass, determined using the fraction of tritium events in the full active volume found within the FV, is 5.5 ± 0.2 tonnes.

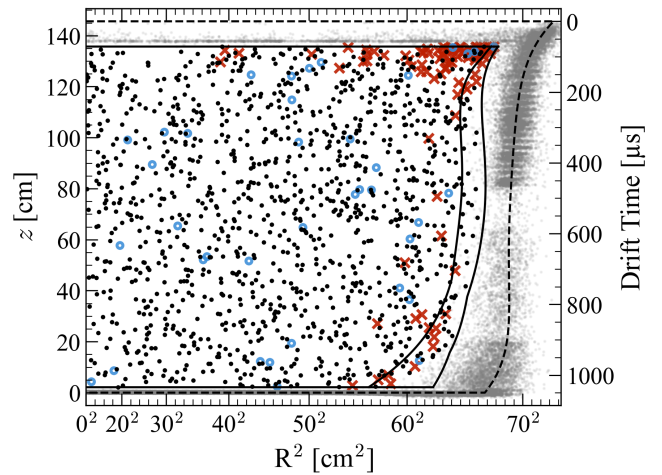


FIG. 1. Data from WS2024, in black with all analysis cuts applied, and in gray outside the FV without veto coincidence cuts. Red crosses and blue circles represent events that are vetoed by the prompt and delayed veto coincidence cuts, respectively. The dashed line shows the active volume, averaged over azimuth, and the two solid lines depict the FV, at the azimuths of its smallest and largest radial extent. The drift field affects the position reconstruction such that the observed radius of the TPC varies as a function of both drift time and azimuthal angle.

Veto coincidence cuts reject events that are accompanied by activity in the Skin and/or OD, and are divided into prompt and delayed categories (see Fig. 1). Prompt cuts target γ rays and fast neutron scatters, removing events with signals in the Skin (OD) of size > 2.5 phd (> 4.5 phd) within 0.25 μs (0.3 μs) of the S1. Delayed veto cuts target neutrons, which thermalize then capture, typically on Gd in the OD with the release of an 8–9 MeV γ -ray cascade. These cuts reject events with pulses in the OD (Skin) of energy $\gtrsim 200$ keV ($\gtrsim 300$ keV) that occur within a 600 μs time window after the S1. The delayed veto cuts remove 3% of the collected live time due to coincidences between unrelated interactions in the TPC and the veto detectors. The veto efficiency for AmLi calibration neutrons, combining prompt and delayed cuts, is measured to be $89 \pm 3\%$. Radiogenic neutrons can be vetoed more effectively as they are typically higher in energy than those from AmLi, and are often accompanied by other neutrons and γ rays. Simulations tuned on the AmLi calibration data indicate that the efficiency to reject background neutrons is $92 \pm 4\%$, with the uncertainty driven by residual discrepancies between the simulations and AmLi data.

Cuts based on S1 and S2 pulse characteristics target accidental coincidence events, in which the random pairing of pulses classified as S1s and S2s mimic true SS interactions. Several sources give rise to isolated S1- and S2-classified pulses, such as interactions in light- or charge-insensitive regions of the detector, spurious

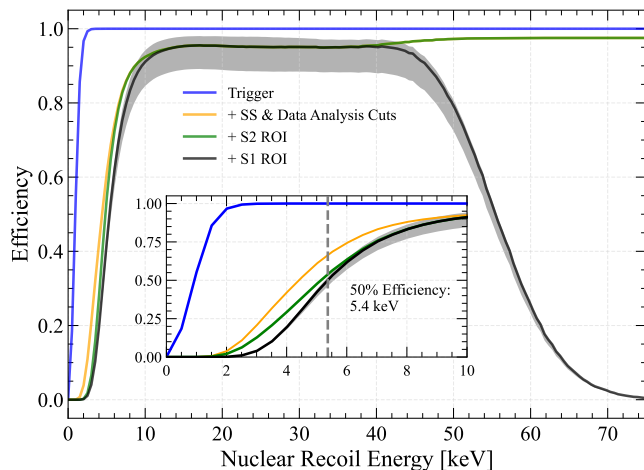


FIG. 2. Energy-dependent NR signal efficiency in WS2024 after the application, in sequence, of the S2 trigger (blue); SS reconstruction and analysis cuts (orange); S2 ROI (green) followed by the S1 ROI (black). The inset shows the low-energy behavior, with the dotted line at 5.4 keV marking 50% efficiency. The uncertainty band (gray) is assessed using AmLi and tritium data as discussed in the text.

Cherenkov photon emissions, or delayed emissions of electrons [19, 20]. The cuts primarily exploit the shapes of these pulses in assessing the validity of the S1-S2 pair. The rejection power of the cuts is evaluated on a sideband of known accidental coincidence events with unphysical drift times ($>1100 \mu\text{s}$) and is 99.5% for all such events in the WIMP ROI.

Live time exclusions discount periods with higher-than-average incidences of accidental coincidences due to elevated pulse rates, which generally occur in the wake of high-energy interactions. A time hold-off is imposed after large S2 signals, dependent on their size, to avoid subsequent delayed ionization or correlated light emission. The hold-off calculation is optimized with respect to that used in WS2022 so that it cumulatively removes 10% of the recorded live time in WS2024, as opposed to 30% in WS2022. Accounting for all live-time losses and exclusions, 81.5% of the collected live time of WS2024 remains for analysis, totaling 220.0 live days.

The cumulative effect of the data selection, event detection, and reconstruction efficiencies on the NR signal efficiency can be seen in Fig. 2, where the cut acceptances are assessed on a combination of tritium and neutron calibration data sets. Uncertainties arise from the combined statistical error on the SS efficiency and data analysis cuts, as well as a systematic error equal to the variation in efficiency of data analysis cuts as evaluated on the different calibration data sets.

To mitigate analyzer bias, artificial, WIMP-like events are injected at random times into the data pipeline, a process referred to as “salting.” Salt events are pre-generated by combining S1 and S2 pulses from sequestered tritium

and AmLi calibration data sets. The pulse sizes for a given event are chosen to best match those expected from an NR energy deposition drawn from a parent distribution consisting of the sum of an exponential (WIMP-like) and a flat spectrum. The salt injection rate and parameters of the parent energy distribution were generated randomly within predefined bounds and kept hidden for the entirety of the analysis. Eight salt events were injected, of which one was removed by analysis cuts, consistent with the NR signal efficiency. The other seven events were revealed as salt following the final definition of the data selection criteria and the likelihood models.

The 1220 events which remain in the 3.3 tonne-year exposure of WS2024 after the application of all data selections and salt removal are shown in Figs. 1 and 3. These events are analyzed using a likelihood model in the $\{S1c, \log_{10}(S2c)\}$ observables. Signal and background model distributions are generated using NEST and event simulations [21], with the exception of the accidental coincidence background model, which follows a data-driven method identical to that used for the WS2022 result [22]. The primary backgrounds and their treatment are similar to those of the WS2022 analysis, with the expected counts for each background source given in Table I. Notable differences are now described.

Two sources of background NR events are considered: those originating from neutrino interactions and those from radioactive decays in detector components. The neutrino interactions are from $\text{CE}\nu\text{NS}$ of solar (^8B and ^7Be) and cosmic-ray-generated atmospheric neutrinos. Nuclear recoils that originate from spontaneous fission and (α, n) reactions in detector materials can be vetoed by detecting the scattered neutrons and/or associated γ rays in the Skin and/or OD. Events vetoed by these systems are used as a sideband that is used to derive an *in-situ* constraint on the number of neutron events in the WIMP search data. As discussed later, the sideband is incorporated directly into the final statistical analysis; however, a sideband-only fit returns an expectation of $0^{+0.2}$ SS counts, as shown in Table I. Secondary estimates from simulations based on detector material radioassays and from data using candidate MS neutron events tagged by the veto detectors return expectations of 0.05 ± 0.01 and 0.3 ± 0.2 neutron counts, respectively, consistent with the primary analysis.

Electron capture (EC) and double electron capture (DEC) decays deposit their energy via X ray and Auger cascades in a more localized profile than a β particle of the equivalent energy, leading to higher ionization densities and enhanced electron-ion recombination. As a result, EC and DEC events look more NR-like than β decays, as reported in Ref. [23]. Preliminary measurements of this effect for ECs in LZ were performed with sidebands of Skin-tagged and multiple scatter decays of ^{127}Xe and ^{125}Xe , isotopes that have been produced *in situ* via neutron activation. These yield a charge-yield

ratio of $Q_y^L/Q_y^\beta = 0.87 \pm 0.03$ for 5.2 keV L-shell EC decays relative to β decays of the same energy.

Two-neutrino DEC decays of ^{124}Xe are observed in LZ with a half-life of $T_{1/2} = (1.09 \pm 0.14_{\text{stat}} \pm 0.05_{\text{sys}}) \times 10^{22} \text{ yr}$ [24], consistent with that in Ref. [25]. The expected number of ^{124}Xe counts in the ROI is estimated assuming an abundance of 9.52×10^{-4} [26] and branching ratios for the LL (10.00 keV) and LM (5.98 keV) decay modes of 1.4% and 0.8%, respectively. The LM charge suppression is modeled with the same ratio of 0.87 as used for single EC decays. The overlap of two L-shell cascades in LL-shell capture should result in additional recombination. As an independent measurement of the LL-shell charge yield is not available, the Thomas-Imel (TI) box model [27, 28] is invoked to relate the ionization density to the amount of electron-ion recombination at a given applied electric field. The ratio of the charge yield for LL-shell DEC to β decays of the same energy, $Q_y^{\text{LL}}/Q_y^\beta$, is treated as a free parameter in the statistical analysis, bounded on one side by the measured Q_y^L/Q_y^β for WS2024 (0.87) and on the other by the result from a preliminary study of increasing the ionization density in the TI box model (0.65).

The largest ER background contribution in this exposure comes from β -emitting isotopes in the LXe bulk. Xenon sampling measurements indicate a concentration of $1.10 \pm 0.18 \text{ ppb } ^{\text{nat}}\text{Ar g/g}$ and an exposure-averaged concentration of $186 \pm 26 \text{ ppq } ^{\text{nat}}\text{Kr g/g}$. These are used to estimate the contributions of ^{39}Ar and ^{85}Kr , respectively. Exposure in the high-mixing state includes residual tritium and ^{14}C activity following calibrations, and therefore both their beta spectra are incorporated into the background model for this period.

Radon emanates from materials exposed to xenon, dispersing in the active volume. With a measured FV activity of $3.9 \pm 0.4 \text{ } \mu\text{Bq/kg}$, ^{214}Pb decays from the ^{222}Rn chain, in particular those to the ground state, form the dominant ER background. A method to identify events with high likelihood of being a ^{214}Pb decay — the radon tag — is developed using simulations of the movement of daughter atoms and ions built from observed flow vectors between ^{222}Rn - ^{218}Po α -decay pairs. A tag volume in which it is probable to find a ^{214}Pb decay is defined for each identified ^{218}Po alpha decay, co-moving with the projected flow streamline for 81 min or approximately $3 \times$ the ^{214}Pb half-life. The radon tag is applied in the low-mixing state, where the flow can be modelled, and when data are available for a continuous 81 min period such that tag volumes can be constructed. For WS2024, the radon tag identifies 15% of the tag-active exposure as ^{214}Pb -rich, containing on average $60 \pm 4\%$ of the ^{214}Pb , estimated directly by measurements of its excited-state decays. The effective ^{214}Pb activity in the untagged remainder of the tag-active exposure is thus $1.8 \pm 0.3 \text{ } \mu\text{Bq/kg}$. Both the radon-tagged and untagged

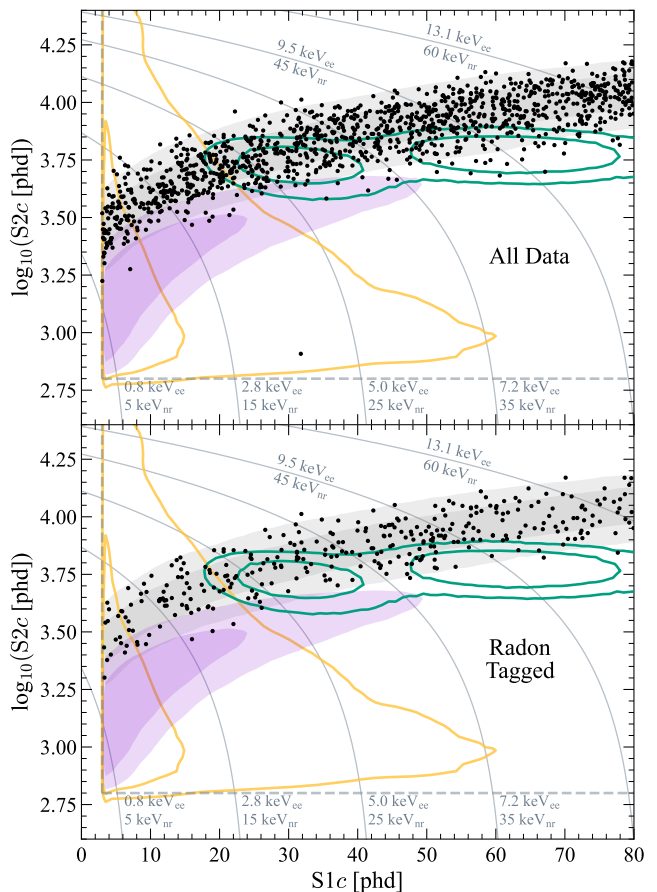


FIG. 3. Black points show the final set of events passing all selection cuts with the panels distinguishing all events in WS2024 (top) from those that are radon tagged (bottom). The radon-tagged data set contains 60% and 15% of the full FV activity of the ^{214}Pb and dispersed backgrounds, respectively; thus the comparison with all data brings to prominence the non- ^{214}Pb backgrounds like ^{124}Xe that are not well-described by the ER band. Dark and light, gray and purple shading show the regions containing 68% and 95% of the ER portion of the background model and a $40 \text{ GeV}/c^2$ WIMP, respectively. Green and orange contours show the same quantiles for the best-fit ^{124}Xe distribution and the accidental coincidence events, respectively. Gray lines show contours of constant ER-equivalent (keV_{ee}) and NR-equivalent (keV_{nr}) energy.

data sets are used in the final WIMP analysis; the former can be seen alongside all the WIMP search data in the bottom panel of Fig. 3. The separation into ^{214}Pb -rich and ^{214}Pb -poor exposures offers the benefit of being able to better identify and constrain other background contributions, ^{124}Xe in particular.

The data are divided into six mutually exclusive samples, which are simultaneously fit using an unbinned, extended maximum likelihood. Five of these apply to the new 220 live-day exposure and describe: (1) events acquired in the high-mixing state; (2) events acquired in

TABLE I. The expected and best-fit counts for different sources in the 3.3 tonne-year exposure of WS2024, including a 40 GeV/ c^2 WIMP signal. Flat β -decay components have been separated based on whether they are affected by the flow state or the radon tag, and the neutron counts are derived *in situ*. “Det. γ s” refers to γ -ray contributions from detector materials, whose Compton spectra are also flat in the ROI.

Source	Pre-fit Expectation	Fit Result
$^{214}\text{Pb } \beta\text{s}$	743 ± 88	733 ± 34
$^{85}\text{Kr} + ^{39}\text{Ar } \beta\text{s} + \text{det. } \gamma\text{s}$	162 ± 22	161 ± 21
Solar ν ER	102 ± 6	102 ± 6
$^{212}\text{Pb} + ^{218}\text{Po } \beta\text{s}$	62.7 ± 7.5	63.7 ± 7.4
Tritium + $^{14}\text{C } \beta\text{s}$	58.3 ± 3.3	59.7 ± 3.3
$^{136}\text{Xe } 2\nu\beta\beta$	55.6 ± 8.3	55.8 ± 8.2
$^{124}\text{Xe DEC}$	19.4 ± 3.9	21.4 ± 3.6
$^{127}\text{Xe} + ^{125}\text{Xe EC}$	3.2 ± 0.6	2.7 ± 0.6
Accidental coincidences	2.8 ± 0.6	2.6 ± 0.6
Atm. ν NR	0.12 ± 0.02	0.12 ± 0.02
$^8\text{B} + \text{hep } \nu$ NR	0.06 ± 0.01	0.06 ± 0.01
Detector neutrons	$^a 0.0^{+0.2}$	$0.0^{+0.2}$
40 GeV/ c^2 WIMP	—	$0.0^{+0.6}$
Total	1210 ± 91	1203 ± 42

^a The expected number of neutron events results from a fit to the sample of veto detector-tagged events. This expectation is not explicitly used in the final combined fit as this sample is included directly in the likelihood, as described in the text.

the low-mixing state when the radon tag was inactive; events acquired in the low-mixing state that are (3) radon tagged, and (4) radon untagged; and (5) events tagged by the Skin or OD. The nuisance parameters, which float within their uncertainties, are the expected number of events for each background source, listed in Table I; the radon tagging efficiency; the neutron veto tagging efficiency; and the $^{124}\text{Xe } Q_y^{\text{LL}}/Q_y^{\beta}$, bounded between 0.65 and 0.87. Parameters characterizing ^{222}Rn and ^{220}Rn daughter backgrounds, tritium and ^{14}C are independent in the high- and low-mixing state exposures. The sixth sample in the likelihood represents WS2022, containing the data and models from the first, 60 live-day WIMP search result [8].

The best-fit number of WIMPs at all masses tested (between 9 GeV/ c^2 and 100 TeV/ c^2) for the combined WS2024+WS2022 analysis is zero. The goodness of fit of the background-only model is assessed in binned 1D projections of the data and model into $S1c$, $\log_{10}(S2c)$, reconstructed energy, distance from the ER band median, as well as the 2D space of $\{S1c, \log_{10}(S2c)\}$. All samples show excellent model-data agreement, passing a Holm-Bonferroni test [29] with a significance level of 0.05. Figure 4 shows the WS2024 data and model in the 1D projection along the ER band median, illustrating the level of agreement through the tails of the distribution with the inclusion of the modified ^{124}Xe response. The fitted values of the radon tagging efficiency and the ^{124}Xe

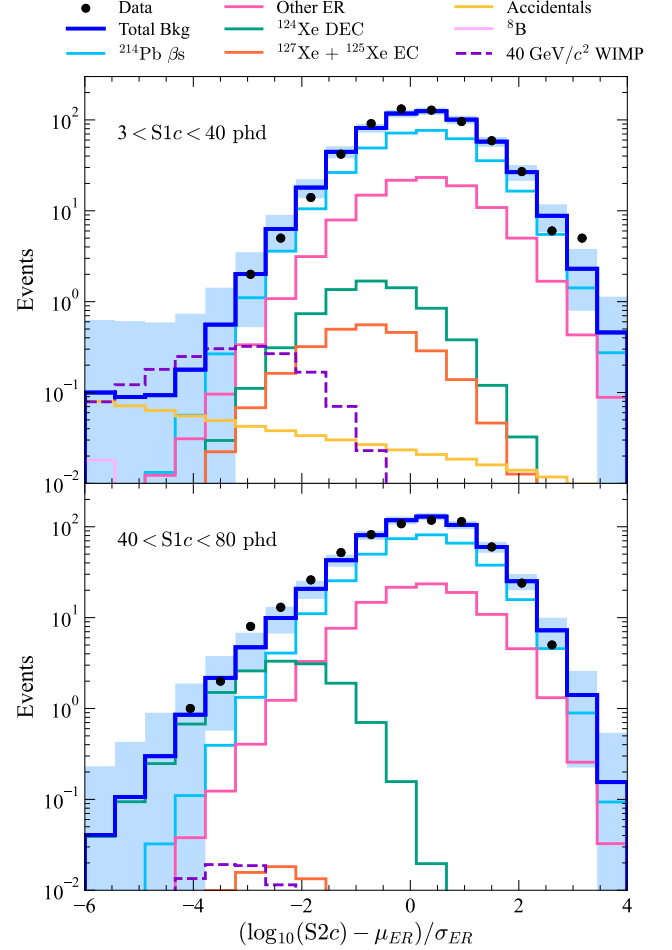


FIG. 4. Comparison between data and the best-fit model for WS2024 corresponding to the values shown in Table I for a background plus a 40 GeV/ c^2 WIMP signal fit in a projection along the ER band median, normalized to the 1σ band width. The 40 GeV/ c^2 WIMP component is shown with an amplitude equal to its power-constrained 90% C.L. upper limit. The upper and lower panels select the $S1c$ ranges 3–40 phd and 40–80 phd with p values of 0.91 and 0.27, respectively. Shaded bands depict the central interval containing 68% of the combined systematic and statistical uncertainties of the model.

$Q_y^{\text{LL}}/Q_y^{\beta}$ are consistent across all masses, at $62 \pm 3\%$ and 0.70 ± 0.04 , respectively, in agreement with the pre-fit expectations.

Figure 5 shows the 90% confidence level upper limit on the spin-independent WIMP-nucleon cross section as a function of mass following inference performed with a two-sided, unbinned profile likelihood ratio test statistic [30]. The limit is power constrained at all WIMP masses to 1σ below the median expectation following the recommendation of Ref. [31]. The fluctuation, and therefore the size of the constraint, is largest between 20 and 50 GeV/ c^2 . This is a consequence of the inclusion of the WS2022 data from Ref. [8], which exhibit an underfluctu-

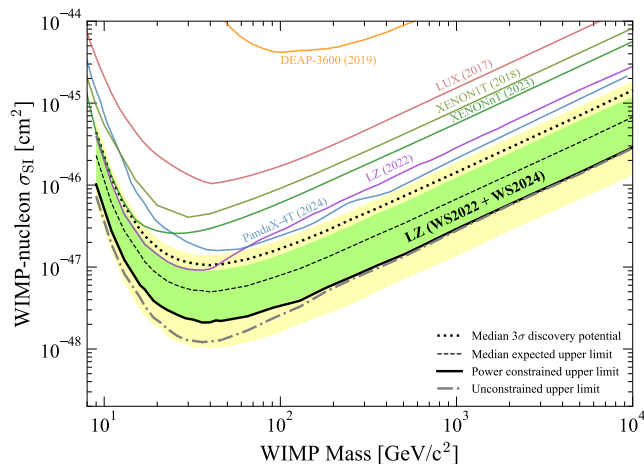


FIG. 5. Upper limits (90% C.L.) on the spin-independent WIMP-nucleon cross section as a function of WIMP mass from the combined WS2024+WS2022 analysis (280.0 live days) are shown with a solid black line, with a -1σ power constraint applied. The gray dot-dash line shows the limits without the power constraint; green and yellow regions show the range of expected upper limits from 68% and 95% of background-only experiments, while the dashed black line indicates the median expectation, obtained with post-fit background estimates. The median 3σ observation potential from the post-fit model is shown as a dotted black line. Also shown are limits from WS2022 only [8], PandaX-4T [10], LUX [32], all power constrained to -1σ ; XENONnT [9], reinterpreted with a -1σ power constraint; XENON1T [33], and DEAP-3600 [34].

ation in this region. The limit for the WS2024 data alone can be found in the Supplemental Material, with an approximate -1σ fluctuation across the entire mass range, primarily attributed to an underfluctuation of the accidental coincidence background in the region of largest overlap with expected WIMP distributions. The minimum of the limit curve is $2.1 \times 10^{-48} \text{ cm}^2$ at $36 \text{ GeV}/c^2$ while that of the median expected limit is $5.0 \times 10^{-48} \text{ cm}^2$ at $40 \text{ GeV}/c^2$. The best median 3σ observation potential is $1.1 \times 10^{-47} \text{ cm}^2$ at $40 \text{ GeV}/c^2$. Results of searching for evidence of spin-dependent WIMP-nucleon couplings are discussed in the Appendix.

In summary, LZ has achieved limits on SI WIMP-nucleon interactions that surpass previous best exclusions by a factor of four or more for WIMP masses $>9 \text{ GeV}/c^2$. A radon tag to target the dominant ER background from ^{214}Pb decays has been demonstrated, with potential for optimization that will allow it to have greater impact on the sensitivities of future searches, particularly for physics with potential ER signals. The enhanced electron-ion recombination of ^{124}Xe LL-shell DEC events was noted for the first time, and will be further investigated in future analyses. The experiment continues to take salted data towards a target 1000-day live time that will enable more sensitive searches for WIMP interactions

and other new phenomena.

Acknowledgements - The research supporting this work took place in part at the Sanford Underground Research Facility (SURF) in Lead, South Dakota. Funding for this work is supported by the U.S. Department of Energy, Office of Science, Office of High Energy Physics under Contract Numbers DE-AC02-05CH11231, DE-SC0020216, DE-SC0012704, DE-SC0010010, DE-AC02-07CH11359, DE-SC0015910, DE-SC0014223, DE-SC0010813, DE-SC0009999, DE-NA0003180, DE-SC0011702, DE-SC0010072, DE-SC0006605, DE-SC0008475, DE-SC0019193, DE-FG02-10ER46709, UW PRJ82AJ, DE-SC0013542, DE-AC02-76SF00515, DE-SC0018982, DE-SC0019066, DE-SC0015535, DE-SC0019319, DE-SC0024225, DE-SC0024114, DE-AC52-07NA27344, & DE-SC0012447. This research was also supported by U.S. National Science Foundation (NSF); the UKRI's Science & Technology Facilities Council under award numbers ST/W000490/1, ST/W000482/1, ST/W000636/1, ST/W000466/1, ST/W000628/1, ST/W000555/1, ST/W000547/1, ST/W00058X/1, ST/X508263/1, ST/V506862/1, ST/X508561/1, ST/V507040/1, ST/W507787/1, ST/R003181/1, ST/R003181/2, ST/W507957/1, ST/X005984/1, ST/X006050/1; Portuguese Foundation for Science and Technology (FCT) under award numbers PTDC/FIS-PAR/2831/2020; the Institute for Basic Science, Korea (budget number IBS-R016-D1); the Swiss National Science Foundation (SNSF) under award number 10001549. This research was supported by the Australian Government through the Australian Research Council Centre of Excellence for Dark Matter Particle Physics under award number CE200100008. We acknowledge additional support from the UK Science & Technology Facilities Council (STFC) for PhD studentships and the STFC Boulby Underground Laboratory in the U.K., the GridPP [35, 36] and IRIS Collaborations, in particular at Imperial College London and additional support by the University College London (UCL) Cosmoparticle Initiative, and the University of Zurich. We acknowledge additional support from the Center for the Fundamental Physics of the Universe, Brown University. K.T. Lesko acknowledges the support of Brasenose College and Oxford University. The LZ Collaboration acknowledges the key contributions of Dr. Sidney Cahn, Yale University, in the production of calibration sources. This research used resources of the National Energy Research Scientific Computing Center, a DOE Office of Science User Facility supported by the Office of Science of the U.S. Department of Energy under Contract No. DE-AC02-05CH11231. We gratefully acknowledge support from GitLab through its GitLab for Education Program. The University of Edinburgh is a charitable body, registered in Scotland, with the registration number SC005336. The assistance of SURF and its personnel in providing physical access and

general logistical and technical support is acknowledged. We acknowledge the South Dakota Governor's office, the South Dakota Community Foundation, the South Dakota State University Foundation, and the University of South Dakota Foundation for use of xenon. We also acknowledge the University of Alabama for providing xenon. For the purpose of open access, the authors have applied a Creative Commons Attribution (CC BY) license to any Author Accepted Manuscript version arising from this submission. Finally, we respectfully acknowledge that we are on the traditional land of Indigenous American peoples and honor their rich cultural heritage and enduring contributions. Their deep connection to this land and their resilience and wisdom continue to inspire and enrich our community. We commit to learning from and supporting their effort as original stewards of this land and to preserve their cultures and rights for a more inclusive and sustainable future.

Appendix - Spin Dependent Results

In this Appendix we report limits on the spin-dependent WIMP-nucleon cross section using the same data selection, background modeling, and statistical inference techniques described in the main text. Results follow an identical procedure to that in Ref. [8]: signal models which describe scattering on ^{129}Xe (spin 1/2, 26.4% natural abundance) and ^{131}Xe (spin 3/2, 21.2% natural abundance) [37] are constructed using the neutron- and proton-only nuclear structure functions and their uncertainties from Refs. [38–40]. The nominal limits use the mean structure functions from [38] and allow for a consistent comparison with previous limits from xenon-based experiments. As in Ref. [8], an uncertainty band is calculated at each WIMP mass using the extrema of power-constrained limits obtained from the minimum and maximum nuclear structure function uncertainties provided in Refs. [38–40].

The best-fit number of WIMP events is zero at all tested masses, from 9 GeV/c^2 to 100 TeV/c^2 . The black line of Figure 6 shows the 90% confidence level nominal upper limit on the WIMP-neutron spin-dependent cross section as a function of mass, while the gray band shows the nuclear structure function uncertainty on the limit. The minimum of the limit curve occurs at 46 GeV/c^2 at a cross section of $\sigma_{\text{SD}}^n = 3.7 \times 10^{-43} \text{ cm}^2$ (median expected limit at $8.5 \times 10^{-43} \text{ cm}^2$ at 40 GeV/c^2), and a power constraint is applied at all tested masses. Figure 7 shows the same for the WIMP-proton spin-dependent cross section. The minimum of the limit curve is at 40 GeV/c^2 at a cross section of $\sigma_{\text{SD}}^p = 9.8 \times 10^{-42} \text{ cm}^2$, and a power constraint is applied between 9 GeV/c^2 and 91 GeV/c^2 . The minimum of the median expected limit on σ_{SD}^p is $2.3 \times 10^{-41} \text{ cm}^2$ and occurs at 40 GeV/c^2 .

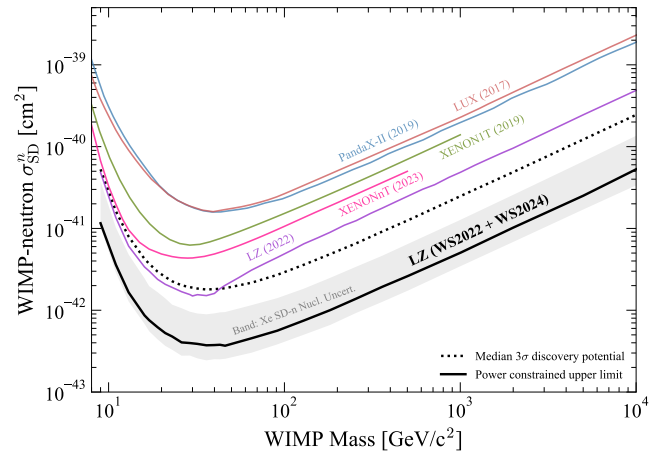


FIG. 6. The 90% confidence-level upper limit (solid-black curve) using the mean of the nuclear structure functions from [38], allowing for like-to-like comparison with other results. The gray band indicates the uncertainty due to nuclear modeling across models from [38–40] and applies similarly to the limit from all xenon-based experiments. The dotted line shows the median 3σ observation significance from the post-fit model. Also shown are the WS2022 only [8], XENONnT [9] (reinterpreted with a -1σ power constraint), XENON1T [41], PandaX-II [42], and LUX [43] limits.

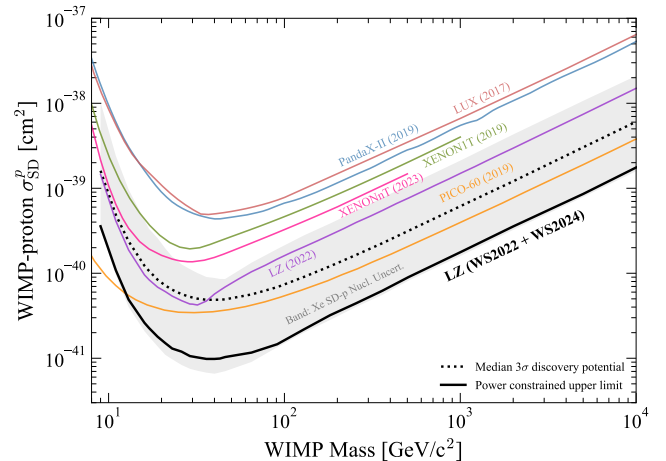


FIG. 7. The 90% confidence-level upper limit (solid-black curve) using the mean of the nuclear structure functions from [38], allowing for like-to-like comparison with other results. The gray band indicates the uncertainty due to nuclear modeling across models from [38–40] and applies similarly to the limit from all xenon-based experiments. The dotted line shows the median 3σ observation significance from the post-fit model. Also shown are the PICO-60 [44], LZ WS2022 only [8], XENONnT [9] (reinterpreted with a -1σ power constraint), XENON1T [41], PandaX-II [42], and LUX [43] limits. The PICO-60 result relies on WIMP-scattering on the spin of the unpaired proton of ^{19}F with minimal uncertainty.

* a.cottle@ucl.ac.uk

† haselsco@umich.edu

‡ Also at The University of Melbourne, School of Physics, Melbourne, VIC 3010, Australia

- [1] N. Aghanim *et al.* (Planck Collaboration), *Astron. Astrophys.* **641**, A6 (2020).
- [2] Y. Sofue and V. Rubin, *Annu. Rev. Astron. Astrophys.* **39**, 137 (2001).
- [3] D. Harvey, R. Massey, T. Kitching, A. Taylor, and E. Tittley, *Science* **347**, 1462 (2015).
- [4] A. Arbey and F. Mahmoudi, *Prog. Part. Nucl. Phys.* **119**, 103865 (2021).
- [5] G. Bertone and D. Hooper, *Rev. Mod. Phys.* **90**, 045002 (2018).
- [6] J. Billard *et al.*, *Rep. Prog. Phys.* **85**, 056201 (2022).
- [7] D. Akerib *et al.*, arXiv:2203.08084 (2022).
- [8] J. Aalbers *et al.* (LZ Collaboration), *Phys. Rev. Lett.* **131**, 041002 (2023), arXiv:2207.03764 [hep-ex].
- [9] E. Aprile *et al.* (XENON Collaboration), *Phys. Rev. Lett.* **131**, 041003 (2023), arXiv:2303.14729 [hep-ex].
- [10] Y. Meng *et al.* (PandaX-4T Collaboration), *Phys. Rev. Lett.* **127**, 261802 (2021).
- [11] D. S. Akerib *et al.* (LZ), arXiv:1509.02910 (2015), arXiv:1509.02910; B. Mount *et al.*, arXiv:1703.09144 (2017); D. S. Akerib *et al.* (LZ Collaboration), *Nucl. Instrum. Methods Phys. Res. Sect. A* **953**, 163047 (2020).
- [12] E. Aprile *et al.* (XENON Collaboration), *Phys. Rev. D* **110**, 012011 (2024).
- [13] J. Aalbers *et al.* (LZ Collaboration), *Nucl. Instrum. Methods Phys. Res. Sect. A* **1068**, 169712 (2024), 2405.14732.
- [14] C. Faham, V. Gehman, A. Currie, A. Dobi, P. Sorensen, and R. Gaitskell, *J. Instrum.* **10** (09), P09010.
- [15] B. López Paredes, H. Araújo, F. Froberg, N. Marangou, I. Olcina, T. Sumner, R. Taylor, A. Tomás, and A. Vacheret, *Astropart. Phys.* **102**, 56 (2018).
- [16] D. Akerib *et al.* (LZ Collaboration), *Astropart. Phys.* **125**, 102480 (2021).
- [17] J. Aalbers *et al.* (LZ Collaboration), *Journal of Instrumentation* **19** (08), P08027.
- [18] M. Szydagis *et al.*, *Noble Element Simulation Technique*, v2.4.0 (2023).
- [19] P. Sorensen, arXiv:1702.04805 (2017).
- [20] D. S. Akerib *et al.* (LUX Collaboration), *Phys. Rev. D* **102**, 092004 (2020).
- [21] D. S. Akerib *et al.* (LZ Collaboration), *Astroparticle Physics* **125**, 102480 (2021).
- [22] J. Aalbers *et al.* (LZ Collaboration), *Phys. Rev. D* **108**, 012010 (2023).
- [23] D. J. Temples, J. McLaughlin, J. Bargemann, D. Baxter, A. Cottle, C. Dahl, W. Lippincott, A. Monte, and J. Phelan, *Phys. Rev. D* **104**, 112001 (2021).
- [24] J. Aalbers *et al.* (LZ Collaboration), arXiv:2408.17391 (2024), arXiv:2408.17391 [hep-ex].
- [25] E. Aprile *et al.* (XENON Collaboration), *Phys. Rev. C* **106**, 024328 (2022).
- [26] J. R. de Laeter, J. K. Böhlke, P. D. Bièvre, H. Hidaka, H. S. Peiser, K. J. R. Rosman, and P. D. P. Taylor, *Pure and Applied Chemistry* **75**, 683 (2003).
- [27] J. Thomas and D. Imel, *Physical Review A* **36**, 614 (1987).
- [28] M. Szydagis, J. Balajthy, G. Block, J. Brodsky, E. Brown, J. Cutter, S. Farrell, J. Huang, E. Kozlova, C. Liebenthal, *et al.*, arXiv:2211.10726 (2022).
- [29] S. Holm, *Scandinavian Journal of Statistics* **6**, 65 (1979).
- [30] G. Cowan, K. Cranmer, E. Gross, and O. Vitells, *Eur. Phys. J. C* **71**, 1 (2011).
- [31] D. Baxter *et al.*, *Eur. Phys. J. C* **81**, 1 (2021); Here we employ a power constraint which uses the expected sensitivity of the experiment assuming no signal is present.
- [32] D. Akerib *et al.* (LUX Collaboration), *Phys. Rev. Lett.* **118**, 021303 (2017).
- [33] E. Aprile *et al.* (XENON Collaboration), *Phys. Rev. Lett.* **121**, 111302 (2018).
- [34] R. Ajaj *et al.* (DEAP Collaboration), *Phys. Rev. D* **100**, 022004 (2019).
- [35] P. Faulkner *et al.*, *J. Phys. G* **32**, N1 (2006).
- [36] D. Britton *et al.*, *Philos. Trans. R. Soc. A* **367**, 2447 (2009).
- [37] J. R. de Laeter, J. K. Böhlke, P. D. Bièvre, H. Hidaka, H. S. Peiser, K. J. R. Rosman, and P. D. P. Taylor, *Pure Appl. Chem.* **75**, 683 (2003).
- [38] M. Hoferichter, J. Menéndez, and A. Schwenk, *Phys. Rev. D* **102**, 074018 (2020).
- [39] P. Pirinen, J. Kotila, and J. Suhonen, *Nucl. Phys. A* **992**, 121624 (2019).
- [40] B. S. Hu, J. Padua-Argüelles, S. Leutheusser, T. Miyagi, S. R. Stroberg, and J. D. Holt, *Phys. Rev. Lett.* **128**, 072502 (2022).
- [41] E. Aprile *et al.* (XENON Collaboration), *Phys. Rev. Lett.* **122**, 141301 (2019).
- [42] J. Xia *et al.* (PandaX Collaboration), *Phys. Lett. B* **792**, 193 (2019).
- [43] D. Akerib *et al.* (LUX Collaboration), *Phys. Rev. Lett.* **118**, 251302 (2017).
- [44] C. Amole *et al.* (PICO Collaboration), *Phys. Rev. D* **100**, 022001 (2019).
- [45] J. Xu, S. Pereverzev, B. Lenardo, J. Kingston, D. Naim, A. Bernstein, K. Kazkaz, and M. Tripathi, *Phys. Rev. D* **99**, 103024 (2019), arXiv:1904.02885 [physics.ins-det].

Supplemental Materials

Data Samples

Figure S1 shows the WS2024 and WS2022 events passing all data selection criteria grouped in their respective sample in the likelihood. Table S1 lists the exposure for each sample in tonne-years.

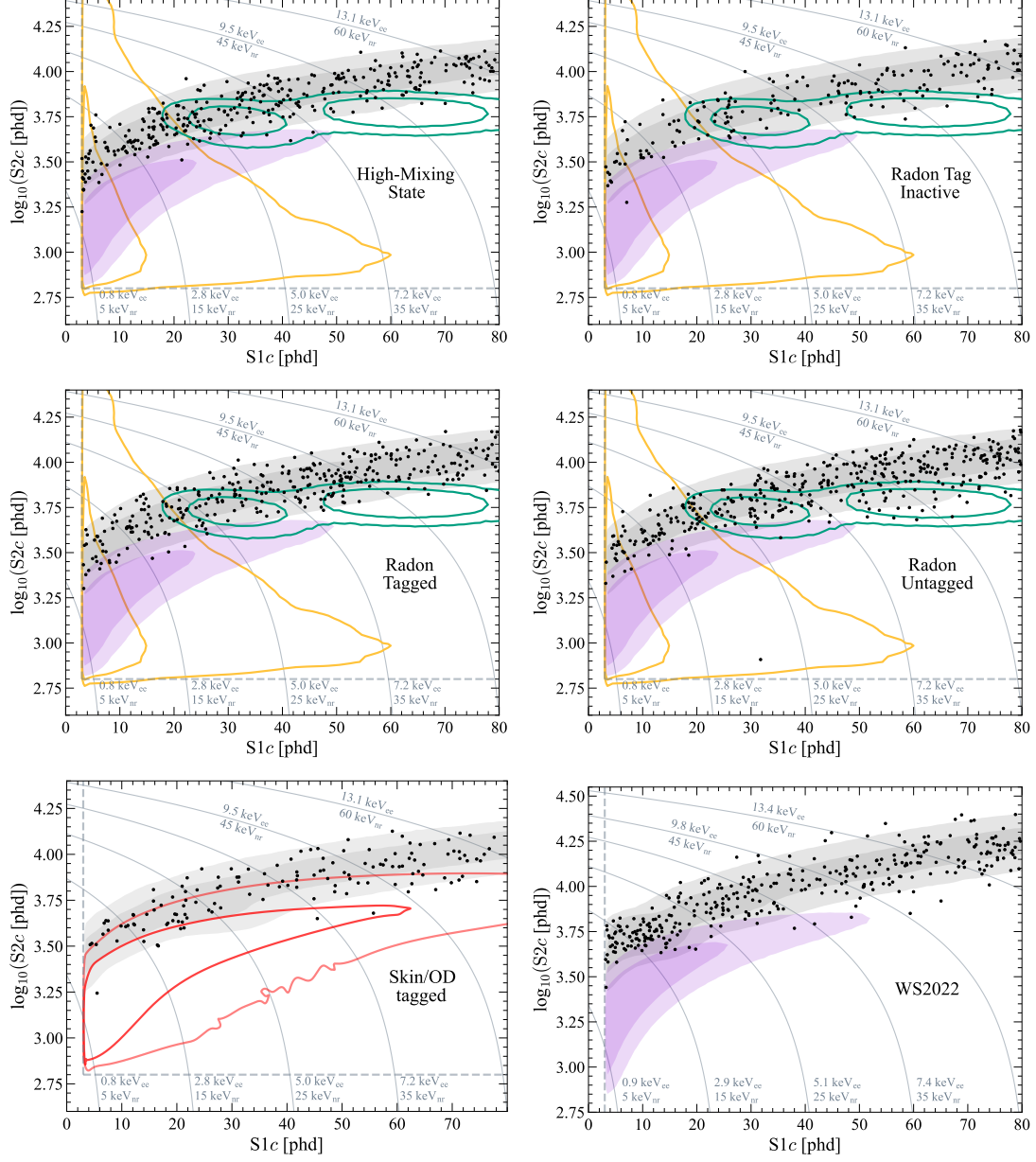


FIG. S1. Panels show the events used in the WS2024+WS2022 combined analysis organized into the various samples described in the main text. Model contours are the same as those in Fig. 3. Red contours in the veto tagged panel display the regions containing 68% and 95% of the distribution of tagged neutron backgrounds.

TABLE S1. Exposures of the six samples used in the likelihood given in tonne-years.

High-Mixing State	Radon Tag Inactive	Radon Tagged	Radon Untagged	Veto Tagged	WS2022 Only
0.6	0.6	0.3	1.8	n/a	0.9

Details of the Detector Response Model

The LZ detector and xenon response models are implemented in a NEST-based application that includes effects such as curved electron drift paths from field non-uniformities, finite position reconstruction resolution in the transverse (x, y) and longitudinal z directions, and position-dependence of the S1 and S2 signal sizes. The key detector parameters of the model are provided in Table S2. A header file for NEST v2.4.0 that reproduce the ER and NR response models used in this analysis is available online at <https://www.hepdata.net/record/155182>.

TABLE S2. Relevant NEST detector parameters. The parameters in the top-half of the table are input parameters, while the bottom-half are results of NEST calculations.

Parameter	WS2024	WS2022
g_1 [phd/photon]	0.112	0.114
g_1^{gas} [phd/photon]	0.076	0.092
Effective GXe Extraction Field [kV/cm]	8.3	8.4
Single Electron Size [phd]	46.9	58.5
Extraction Efficiency [%]	72.5	80.5
g_2 [phd/electron]	34.0	47.1

Note that NEST has multiple models for extraction efficiency versus gaseous xenon (GXe) electric field strength due to conflicting measurements in the literature [S45], and the default model provides the lower bound of the extraction efficiency for a given field strength. In order to reproduce the observed single electron size and measured extraction efficiency in LZ with this default model, a higher effective value for the GXe field magnitude is used, and thus the value reported in Table S2 does not represent a physical field inside the LZ TPC. Extraction efficiency is measured as the ratio between the best-fit electroluminescence gain (g_2) value and the observed single electron signal size.

In addition to the parameters below, the ER and NR mean yield and fluctuations models have been tuned to minimize the discrepancy between NEST and LZ calibration data. The ER mean yield parameters are provided in Table S3, and the NR parameters are shown in Table S4. Nomenclature for the individual parameters follows from [S28]. There are detailed instructions for implementing these changes in the provided file referenced above.

TABLE S3. Default and best-fit model parameters for the NEST ER mean charge yield model. The LZ values were found by fitting to the ^3H and ^{14}C band means. See Eq. 6 of [S28] for more information regarding the individual m_i .

Parameter	NEST Default at 97 V/cm	LZ Value
m_1 [keV $^{-1}$]	14.6	12.5
m_2 [keV $^{-1}$]	77.3	85.0
m_3 [keV]	0.8	0.6
m_4	2.1	2.1
m_5 [keV $^{-1}$]	19.3	25.7
m_6 [keV $^{-1}$]	0	0
m_7 [keV]	78.0	59.7
m_8	4.3	3.7
m_9	0.33	0.28
m_{10}	0.08	0.11

TABLE S4. Model parameters for the NEST NR mean light and charge yields model. The LZ values were found by fitting to the calibrated DD band mean. See Eqs. (10), (12), and (13) of [S28] for more information regarding the individual parameters. The last two parameters (f_1 and f_2) are not described in [S28], but are available as free parameters in NEST, controlling the asymmetry of the sigmoidal energy dependence for the charge and light yields, respectively. See the NEST function GETYIELDNR(...) for the usage of f_1 and f_2 in calculating NR yields [S18].

Parameter	NEST Default	LZ Value
α [keV $^{1/\beta}$]	11.0	10.2
β	1.1	1.1
γ [(V/cm) $^{1/\delta}$]	0.048	0.050
δ	-0.0533	-0.0533
ϵ [keV]	12.6	12.5
ζ [keV]	0.30	0.29
η	2.0	1.9
θ [keV]	0.30	0.32
ι	2.0	2.1
p	0.50	0.51
f_1	1.0	0.996
f_2	1.0	0.999

WS2024-Only Limit

Figure S2 shows the SI WIMP-nucleon cross section upper limit obtained using the data and models pertaining to the WS2024, 3.3 tonne year exposure only.

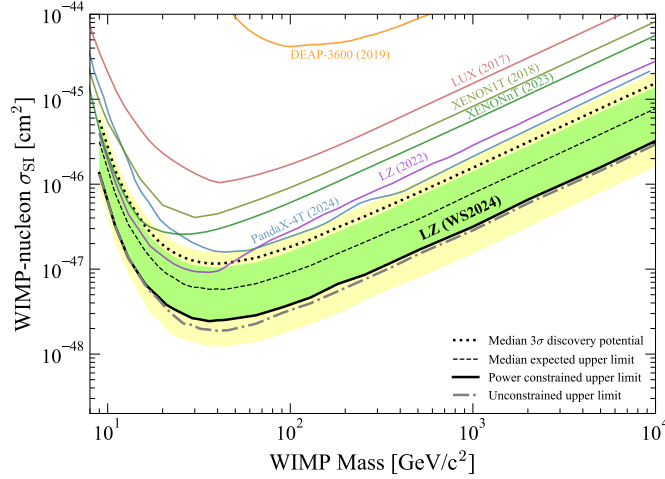


FIG. S2. Upper limits (90% C.L.) on the spin-independent WIMP-nucleon cross-section as a function of WIMP mass from WS2024 (220.0 live days) only are shown with a solid black line, with a -1σ power constraint applied. The gray dot-dash line shows the limits without the power constraint; green and yellow regions show the range of expected upper limits from 68% and 95% of background-only experiments, while the dashed black line indicates the median expectation, obtained with post-fit background estimates. The median 3σ observation significance from the post-fit model is shown as a dotted black line. Also shown are limits from WS2022 only [S8], PandaX-4T [S10], LUX [S32], all power constrained to -1σ ; XENONnT [S9], reinterpreted with a -1σ power constraint; XENON1T [S33], and DEAP-3600 [S34].

Limits in Terms of Number of WIMP Events

Figure S3 presents the WS2022+WS2024 combined and WS2024-only upper limits in number of events.

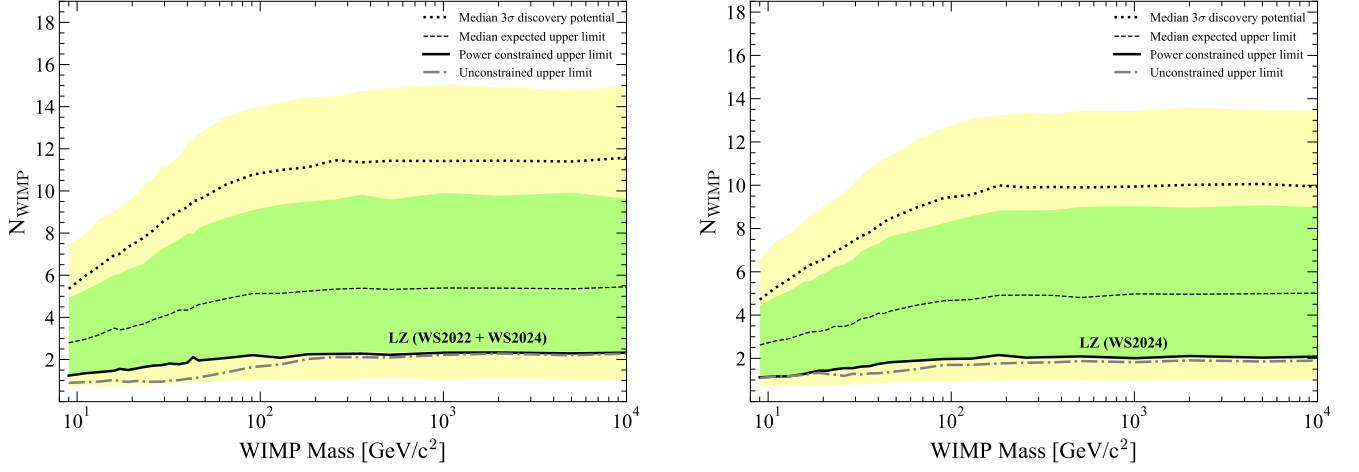


FIG. S3. The 90 % confidence limit (solid line) for the number of WIMP events versus WIMP mass in the spin-independent case for the combined analysis (left) and WS2024 only (right). The dot-dash line shows the limit before applying the power constraint described in the text. The dashed line shows the median sensitivity and the dotted line shows the median 3σ discovery sensitivity. The green and yellow bands are the 1σ and 2σ sensitivity bands.